HHS Public Access

Author manuscript

Cogn Neurosci. Author manuscript; available in PMC 2021 January 01.

Published in final edited form as:

Cogn Neurosci. 2020 January ; 11(1-2): 71–91. doi:10.1080/17588928.2019.1627303.

Cross-Frequency Coupling of Alpha Oscillatory Power to the Entrainment Rhythm of a Spatially Attended Input Stream

Tommy J. Wilson[1,3], **John J. Foxe**[1,2]

[1]The Cognitive Neurophysiology Laboratory, Department of Pediatrics & Neuroscience, Albert Einstein College of Medicine & Montefiore Medical Center, Bronx, NY 10461, USA

[2]The Cognitive Neurophysiology Laboratory, Department of Neuroscience, The Ernest J. Del Monte Institute for Neuroscience, University of Rochester School of Medicine and Dentistry, Rochester, NY 14642, USA

[3]Department of Medicine, Columbia University College of Physicians and Surgeons, Columbia University Medical Center, New York Presbyterian Hospital, New York, NY 10032, USA

Abstract

Neural entrainment and alpha oscillatory power (8-14 Hz) are mechanisms of selective attention. The extent to which these two mechanisms interact, especially in the context of visuospatial attention, is unclear. Here, we show that spatial attention to a delta-frequency, rhythmic visual stimulus in one hemifield results in phase-amplitude coupling between the delta-phase of an entrained frontal source and alpha power generated by ipsilateral visuocortical regions. The driving of ipsilateral alpha power by frontal delta also correlates with task performance. Our analyses suggest that neural entrainment may serve a previously underappreciated role in coordinating macroscale brain networks and that inhibition of processing by alpha power can be coupled to an attended temporal structure. Finally, we note that the observed coupling bolsters one dominant hypothesis of modern cognitive neuroscience, that macroscale brain networks and distributed neural computation are coordinated by oscillatory synchrony and cross-frequency interactions.

Keywords

neural oscillations; entrainment; attention; alpha oscillations; delta oscillations; cross-frequency coupling; phase-amplitude coupling

Introduction

Neural oscillations are thought to coordinate attention and behavior. For instance, delta-frequency stimulation (1–3 Hz) entrains endogenous oscillations in sensory cortex, supporting attentional selection between competing stimuli (Lakatos, Karmos et al. 2008, Besle, Schevon et al. 2011, Gomez-Ramirez, Kelly et al. 2011). With respect to visuospatial attention, we recently observed that delta-frequency entrainment of bilateral visual areas by

Correspondence: john_foxe@urmc.rochester.edu.

a lateralized visual stimulus enables covert attentional selection, despite the concurrent presentation of a strong, competing rhythm in the unattended hemifield (Gray, Frey et al. 2015). However, the study of entrainment is quite nuanced. It requires the demonstration of a pre-existing oscillator that *becomes entrained,* and it is often confounded by stimulus-evoked activity (for a comprehensive review of methodologic considerations, see Keitel, Thut et al. 2017, Zoefel, Ten Oever et al. 2018). Moreover, the interaction between entrainment and stimulus processing may depend on stimulation frequency (e.g. Keitel, Thut et al. 2017).

Spectral power in the alpha band (8–14 Hz) is also tied to attention (Worden, Foxe et al. 2000, Kelly, Lalor et al. 2006, Thut, Nietzel et al. 2006). In visuospatial attention tasks, covert attention to a lateralized visual stimulus increases posterior alpha power ipsilaterally and decreases it contralaterally. Since the ipsilateral hemisphere receives direct input from competing stimuli in the unattended visual field, increases in ipsilateral alpha power support the notion that alpha activity indexes functional suppression of processing (Foxe, Simpson et al. 1998, Jensen and Mazaheri 2010, Foxe and Snyder 2011). While we here emphasize this suppressive account, we note that the interaction between alpha activity and attention is likely more complex than presently appreciated and remains a matter of open inquiry (Palva and Palva 2007, Rohenkohl and Nobre 2011, Gips, van der Eerden et al. 2016, Foster and Awh 2018).

In any case, the relationship between delta-frequency entrainment and alpha power is not straightforward. Lakatos, Barczak et al. (2016) and Henry, Herrmann et al. (2017) argue that the two appear to be generally counter-posed, indicating distinct attentional states or strategies. In contrast, Gomez-Ramirez, Kelly et al. (2011) and Wostmann, Herrmann et al. (2016) demonstrate that the time course of alpha oscillatory power can be modulated at the attended delta frequency, suggesting their co-occurrence is functionally meaningful. However, we caution that these studies employ a mix of auditory and visual stimuli. As such, the extent to which—and indeed whether—they generalize to the specific context of visuospatial attention, where lateralization of alpha power plays a causal role in perception (Romei, Gross et al. 2010), is unclear, and additional investigation on this point is warranted.

To examine the relationship between delta-frequency entrainment and alpha oscillatory power during visuospatial attention, we employ high-density electroencephalography (EEG) during the Spatial Continuous Temporal Expectancy Task (Spatial CTET; Gray, Frey et al. 2015). Surprisingly, we observe that ipsilateral alpha power is coupled to a delta-entrained, frontocentral source and that successful task performance is associated with increased driving of ipsilateral alpha power by frontal delta activity. Our findings underscore the importance of oscillatory mechanisms to visuospatial attention. More generally, they also support a hypothesis of broad significance in modern cognitive neuroscience, that neural oscillations bind distributed neural ensembles into functional, macroscale neural networks.

Methods

Participants

Twenty-seven participants were recruited for a three-day experimental protocol. Concurrent sessions were between one and two weeks apart. Three subjects did not complete the full protocol (2 withdrew voluntarily; 1 was unable to maintain eye-fixation during the task), leaving 24 adults (mean age: 26.5, $\sigma = \pm 3.9$, 11 females, 3 left-handed). Three of the 24 subjects previously participated in a one-day study with an identical task. All subjects had normal or corrected-to-normal vision. One subject was congenitally deaf in one ear, and another had a previous history of depression, albeit not within the past year. No other subjects reported any previous/concurrent neurological or psychiatric conditions. Two subjects routinely took medications (apart from hormonal contraception) during the study: one took Lunesta (eszopiclone) nightly and another took Advil (ibuprofen) as needed. 72 subject-days of data (24 subjects × 3 days) were collected, but 2 of these datasets (one from each of two different individuals) were excluded from further analysis because of recording errors leading to non-existent or incomplete eye-tracking and/or EEG records. All datasets from one of the 24 participants were also rejected outright due to poor data quality, leaving 67 subject-day datasets from 23 participants. All subjects were compensated for each day of the study, totaling $320 in compensation at study completion. Procedures and protocols were approved the by the Institutional Review Board of the Albert Einstein College of Medicine. Ethical standards and decision-making were in accordance with the principles outlined in the Declaration of Helsinki.

Stimuli, Task and Experimental Protocol

On each experimental day, subjects performed mini-blocks of the Spatial Continuous Temporal Expectancy Task (Spatial CTET; Gray, Frey et al. 2015), which requires sustained visuospatial attention for several minutes (generally 3–4, depending on task titration). Subjects covertly attend one of two rotating checkerboard streams and report the appearance of duration deviants (targets) that appear as pauses or breaks in the rotation rhythm. We will here describe the task, but the reader is encouraged to review our recent publications for additional descriptions of the task and characterization of associated neurophysiological findings (Gray, Frey et al. 2015, Wilson, Gray et al. 2018).

As shown in Figure 1, the stimulus consists of a black central fixation dot and two checkerboards presented against a gray background. Each checkerboard was composed of a 10×10 grid of smaller squares; each smaller square was diagonally cut into two triangles colored with different shades of grey (see also Supplementary Methods). One checkerboard rotated every 666.66 ms (1.5 Hz), and the other rotated every 766.66 ms (1.3 Hz), resulting in two, simultaneously-presented streams of temporally predictable, rhythmic visual information. Stimulus configuration (which checkerboard rotated at which frequency) was counterbalanced across mini-blocks. Four checkerboard orientations were possible (0°, 90°, 180° and 270°). To produce each rotation, one of the three orientations not currently occupied by a given checkerboard was chosen at random for its next orientation, resulting in unpredictable apparent rotations of 90° clockwise, 90° counter-clockwise and 180°. Rotations for each stream were chosen independently of the other stream.

Participants were instructed to: maintain central fixation on the fixation dot; attend the prompted checkerboard stream covertly for an entire mini-block; and respond via mouse click with their right index finger whenever they detected a duration deviant. Deviants occurred independently in each checkerboard stream every 8–12 seconds with the number of standards (normal-duration checkerboards) between deviants drawn from a uniform distribution over this time interval. On average, 15 ($\sigma = \pm 2$) standards were shown between deviants. The experimental protocol for day 1 had 27 *unique* mini-blocks (~3–4 minutes each), and participants completed the same 27 mini-blocks in the same order on days 2 and 3. The ordering of standards and targets for each of the 27 mini-blocks was: determined before any participants were enrolled; computed independently for each mini-block and checkerboard stream; and held constant across participants. As a result, the only difference in stimulation between subjects was due to titration of the inserted delay.

At the beginning of the first day of experimentation, participants were presented with a practice block, during which the task was verbally explained. Task difficulty was also titrated at the beginning of the first day with two titration blocks, in which the duration of the deviant was adjusted using a 3-up, 1-down Up-Down Transformation Rule (UDTR). A single miss increased the duration of the target by 33 ms, and 3 hits in a row decreased its duration by the same amount. No additional titration was performed.

The duration of the deviant was longer than that of the standards, as shown in Figure 1. But, until the deviant duration outlasted the standard duration, it could not be identified. This moment of expectancy violation, where a new standard was expected *but did not arrive* because of the added delay, is labeled T_1 (T = 1 standard cycle elapsed). Hits were defined as responses (mouse clicks) that occurred within 1500 ms after T_1. The titrated deviant duration (in excess of T_1) was used for both checkerboard streams in all subsequent blocks. Across all 23 remaining subjects, titration produced deviant durations that exceeded T_1 by 610 ms ($\sigma = \pm 190$ ms) on average and resulted in an average detection rate of 62% ($\sigma = \pm 17\%$) across all participants and experimental days.

Subjects began each day with 2 mini-blocks, after which a short break was given; thereafter, a break was given after every 5 mini-blocks (every 15–20 minutes). Between these larger 5-mini-block segments, participants performed 2 mini-blocks of a foil task similar to the Spatial CTET (results not discussed here). As with stimulus configuration (which checkerboard rotated at which frequency), attended checkerboard (left vs. right) was also counterbalanced across mini-blocks on each day. Total time-on-task was between 80 and 110 minutes per day. A total of 439 attended deviants and 6,819 attended standards were presented per day; thus, the 23 subjects included in the final analysis were each presented with 1,317 deviants and 20,457 standards in the attended streams.

Data Acquisition

EEG data were acquired from 168 sintered Ag-AgCl active electrodes (160 scalp electrodes; 8 external electrodes) with BioSemi ActiveTwo system. Recordings were digitized at 512 Hz and referenced during acquisition to the CMS-DRL convention (Common Mode Sense-Driven Right Leg). During acquisition, signals were bandpass filtered between 0.16 Hz and 100 Hz. To ensure central fixation, eye-tracking data were acquired with an infrared eye-

tracking system (EyeLink 1000 Remote/Head Free Upgrade; SR Research). Eye-tracker data were digitized at 500 Hz. Calibration of the system was performed at the start of the day and after each scheduled break with a nine-point grid. Triggers denoting checkerboard presentation were sent from the stimulus-presentation computer to each of the eye-tracking and EEG acquisition systems to allow for offline synchronization during data processing.

Data Preprocessing

Data were processed offline with MATLAB R2015a and R2016a (The MathWorks) using custom-written scripts and standard EEG toolboxes (EEGLab, Delorme and Makeig 2004, and FieldTrip, Oostenveld, Fries et al. 2011). Because of the size of the full data-set (70 subject-days of data at the start of preprocessing), algorithms for automation of EEG data-processing—including FASTER (Nolan, Whelan et al. 2010) and an automatic ICA-Component classifier based on an optimized feature set (Winkler, Haufe et al. 2011)—were employed. EEG records for each subject-day were processed separately as follows.

Continuous EEG data for each mini-block were concatenated and re-referenced from the CMS-DRL convention to channel A1 (Cz). Data were high-pass filtered at 1 Hz with a digital, 6^{th}-order Butterworth filter with zero phase shift. Bad channels were identified with the FASTER algorithm, resulting in an average of 6 ($\sigma = \pm 3$) bad channels per subject-day. For additional technical details, we refer the reader to Nolan, Whelan et al. (2010; especially Figure 2). Bad channels were interpolated at the end of preprocessing. Data were then down-sampled from 512 Hz to 128 Hz, demeaned and re-referenced to an average of all remaining (good) scalp electrodes.

Artifact Rejection by ICA—For computational efficiency, dimensionality reduction was then performed with principal components analysis, keeping only dimensions that explained >0.001% of the variance. Averaged across the 67 subject-day datasets in the final analysis, this procedure retained 139 ($\sigma = \pm 27$) of the dimensions remaining after bad channel rejection (leaving, on average, 99.99% ($\sigma = \pm 0.01\%$) of variance in the data set). Dimensionality-reduced data then underwent decomposition by independent components analysis with the Extended-Infomax-ICA Algorithm as implemented in the FieldTrip toolbox. The Extended-Infomax-ICA algorithm was chosen as it effectively separates neural signals from both super-Gaussian (eye-blinks, cardiac artifacts) and sub-Gaussian (line noise) sources of noise, unlike the original Infomax-ICA algorithm that is only able to separate super-Gaussian sources (Lee, Girolami et al. 1999).

To isolate artifactual ICA components for rejection, we implemented a linear classifier. In particular, we employed the linear discriminant function available in Matlab's *classify* command, and the feature space for classification was that described by Winkler, Haufe et al. (2011).

Roughly one-third of the subject-day datasets were selected (N = 24 of 70 subject-day datasets) at random to train the classifier. Each training dataset was inspected by hand, and ICA components were visually classified by topography and time course into one of three groups: definite eye-blinks, definite "pop-off" (high activity in a single-channel only) or neither. Components representing blinks and pop-off events were labeled as artifacts. Of the

3,674 components used for training, 1,952 (53%) of them were labeled definitively artifactual, and 1,722 (47%) were labeled as neither definitively eye-blink nor pop-off.

The trained classifier was then applied to all 70 subject-day datasets, including datasets on which the classifier was trained. Each component from every dataset was therefore classified as definitively artifactual or not. All assignations were visually inspected for quality control. At this point, all 3 subject-day datasets for one subject were discarded because of poor data quality. Of the remaining 67 datasets, an average of 84 (σ = ± 22) ICA components were labeled as artifactual and discarded. Consequently, an average of 54 (σ = ± 23) non-definitive ICA components remained for remixing (recombination) into electrode-space (60% variance remaining, σ = ± 20%).

After recombination, each block of EEG data was epoched into trials relative to deviants that appeared in both the left and right checkerboard streams, regardless of which was attended in a given mini-block. Epochs were defined as the interval from t = −8 seconds to t = 2 seconds, where t = 0 corresponds to the onset of each deviant. However, only the interval from t = −8 seconds to t = 0.9 seconds was used for final analysis, since t = 0.9 seconds was the shortest titrated deviant—i.e. the earliest moment at which any one of the subjects was presented with a new standard after deviant onset at t = 0.

Epoch Rejection and Channel Interpolation—All EEG and eye-tracking data from each of the epochs were then analyzed. Any trials that did not contain a full 10 seconds of EEG data (t = [−8,2] seconds) were removed, amounting in an average loss of 12 (σ = ±2) trials per subject-day. To ensure that fixation was maintained in each epoch, trials were rejected if a subject's gaze deviated by >2.5° horizontally or vertically for >400 ms. We also rejected trials that contained >1000 ms worth of horizontal or vertical deviations >2.5°, even if none of these deviations were individually >400 ms in duration. Across 67 subject-days, an average of 155 (σ = ±148) trials were rejected because fixation was not maintained. These criteria ensured that any differences between attend left and attend right conditions were due to *covert* attention (i.e. differences were *not* due to overt eye-movements). An average of 20 trials (σ = ±10) per subject-day were then rejected by the FASTER epoch rejection algorithm (Nolan, Whelan et al. 2010).

Channels previously identified as bad were spline interpolated in every epoch as per the *h_eeg_interp_spl* function available in the FASTER toolbox, which is based on the *eeg_interp* function in the EEGLAB toolbox. Finally, each epoch itself was itself searched for bad channels as per FASTER, which resulted in rejection and spline interpolation of 6.1 (σ = ±2.0) channels from each epoch. After preprocessing, 660 (σ = ±150) trials—including both attended and unattended trials—remained per subject-day.

Data Analysis

Delta Filtering and Alpha Envelopes—Delta-filtered activity for each trial was computed by bandpass filtering from 1–2 Hz (4th-order Butterworth filter, zero phase shift). Importantly, filtering took place after ICA recombination but before trial epoching to avoid edge artifacts. Delta-filtered trials were preprocessed in the same manner as their broadband

counterparts; in particular, if a broadband trial was rejected (or one of its channels interpolated), its delta-filtered equivalent underwent the same.

Alpha envelope data for each trial were computed in a similar fashion. However, in this case, a bandpass filter between 8–12 Hz was applied (4^{th}-order Butterworth filter, zero phase shift), followed by the Hilbert transform to compute instantaneous amplitude (see FieldTrip function *ft_preproc_hilbert*, option: abs). To baseline-correct alpha envelopes, a 1 Hz high-pass filter was applied (6^{th}-order Butterworth filter, zero phase shift). As with delta-filtered data, extraction of envelopes occurred before trial epoching to avoid edge artifacts, and alpha envelopes underwent the same rejection/interpolation steps as their broadband counterparts.

Timeseries Analysis—Cluster-based, non-parametric randomization testing via FieldTrip's *ft_timelockstatistics* function (method: montecarlo, correct: cluster) was used for statistical analysis. All images were masked by cluster-corrected significance ($p < 0.05$) unless otherwise specified. Exposition regarding additional statistical testing is given where appropriate in the Results section. Three additional time-series operations warrant explicit discussion: collapse to a common domain (cycles elapsed); mirroring of alpha envelope data; and measurement of delta-filtered phase.

When a checkerboard rotated at 1.5 Hz, standards were presented at t = …−2, −1.333, −0.666 s. When rotating at 1.3 Hz, standards were presented at t = …−2.3, −1.533, −0.766 s (deviant onset is t = 0 s). To align stimulation timing for both frequencies, we converted them to a common domain: cycles elapsed (T). For conversion, the time of each event (in seconds) was simply multiplied by the frequency of stimulation. Then, for both cases (1.5 and 1.3 Hz), standards were presented at T = …−3, −2, −1. By this nomenclature, T_0 (T = 0) denotes the initial presentation of the duration deviant, whereas T_1 (T = 1) marks the moment where checkerboard rotation was expected but *did not occur* because of the inserted delay (also see Figure 1). As preprocessed trials were sampled every 7.8 ms (1/128 Hz), 1.5 Hz trials were sampled (on average) just over 85 times between T_0 and T_1 (666.66/7.8), whereas 1.3 Hz trials were sampled just over 98 times (766.66/7.8). To overcome this discrepancy, we linearly interpolated the 1.5 Hz trials at those time points sampled in the 1.3 Hz trials before analysis. We were then able to average across stimulus configuration readily, as both configurations shared the same domain and sample timing. Limited analysis without conversion to a common domain and interpolation is included in the Supplementary Figures.

Since alpha lateralization depends on which side of space is attended, we were interested in alpha activity *relative to the checkerboard of interest* (i.e. *ipsilateral* or *contralateral* to the epoching checkerboard, not left or right in an absolute sense). To organize the data in this framework, we took trials epoched to the stimulus stream in the right hemifield and mirrored them across the sagittal plane. Sensors right of midline were mapped to their mirrored spots left of midline (and vice versa). Data from left (non- mirrored) and right (mirrored) trials were then averaged. Consequently, all ipsilateral data (i.e. data from sensors ipsilateral to the epoching checkerboard) were found in sensors left of midline, whereas contralateral data were found in those right of midline.

To examine the relationship between delta activity and behavior, we explicitly computed instantaneous delta phase by Hilbert transforming the delta-filtered data (*ft_preproc_hilbert*, option: angle). Delta phases at T_1 and on presentation of unattended standards (see Methods, Data Analysis, Unattended Visually Evoked Potential (VEP) Analysis) were extracted for the analyses in Figure 5; delta phases throughout the entire trial were extracted for analysis in Figure 7.

Spectral Analysis—Both broadband trial data and alpha envelope data underwent Fourier decomposition via *ft_freqanalysis* (method: mtmfft). For these analyses, data from t = −8 to t = 0.9 seconds were padded to 10 seconds in length and windowed by a Hanning taper before frequency decomposition. Power spectra were computed in two ways for each data set, namely: before and after averaging (complex) Fourier spectra across trials. In the former, broadband activity was observed, although this activity was not necessarily in-phase across trials (Supplementary Figures 4 and 9); the latter approach highlighted activity that was in-phase across trials (Supplementary Figures 3 and 8). Topographies of power distribution at the stimulus frequency were subsequently generated.

Unattended Visually Evoked Potential (VEP) Analysis—To isolate VEPs in response to unattended standards, we subjected the broadband data to a high-pass filter at 2 Hz (6^{th} order Butterworth filter, zero phase shift) immediately after ICA recombination. We then epoched with respect to standards presented in the unattended checkerboard stream. In this context, high-pass filtering effectively removes the low-frequency activity (read: delta activity) demonstrated in Figure 2; however, the VEP, whose spectral power is principally concentrated above 2 Hz, is unaffected.

Before plotting, VEPs were: baseline corrected from −100 to 0 ms, where 0 ms is defined to be the onset of the unattended standard; concatenated across all checkerboard hemifield × checkerboard rotation frequency combinations; and collapsed across the depicted gray sensors in Figure 5, *Middle*. These sensors were chosen because the VEP distributes bilaterally across posterior scalp sites (Gonzalez, Clark et al. 1994, Foxe, Doniger et al. 2001, Di Russo, Martínez et al. 2002).

Source Localization—Source localization of EEG data was computed in both time and frequency domains with the eLORETA algorithm (*ft_sourceanalysis*, method: eloreta). In all cases, we utilized a template MRI and BEM headmodel (Holmes, Hoge et al. 1998, Oostenveld, Stegeman et al. 2003, Pascual-Marqui 2007). In Figures 3 and 4 (and Supplementary Figure 5), broadband trial data were used to construct covariance matrices, which were collapsed across checkerboard hemifield (left vs. right) before source-fitting. Binary masks were then generated by thresholding the resulting three-dimensional datasets. By averaging dipole power across these masks at each time point, source time-courses were reconstructed.

In Figure 6, alpha activity was localized in the frequency domain. Broadband trial data was first wavelet transformed in the alpha band (*ft_freqanalysis*, method: wavelet, foi: 11, width: 4) to compute cross-spectral density (CSD) at each electrode pair. Subsequently, data epoched to the right checkerboard were mirrored as in the Timeseries Analysis section above

before collapse across checkerboard hemifield. Source analysis followed, and source power was computed with binary masking as before. To generate the contrast in Figure 6, *Bottom Right*, this procedure was executed with CSDs generated from both: 1. the entire plotted interval in Figure 6, *Bottom Left*; and 2. the T_1 interval alone (T = 0.715 to T = 1.17; dashed black box). The final contrast was then composed as: ($P_{att,T1}$ - $P_{att,full}$) - ($P_{unatt,T1}$ - $P_{unatt,full}$), where $P_{att,T1}$ reflects source power during the attended condition with CSD computed from the T_1 interval (and so forth). In this way, the generated contrast captures how alpha power on the T_1 interval decreases from baseline as a function of attention.

Phase-Slope Index—For causal analysis, we employed the normalized Phase-Slope Index (PSI; Nolte, Ziehe et al. 2008, Jiang, Bahramisharif et al. 2015); in particular, we used the implementation in *ft_connectivityanalysis* (method: psi). Briefly, PSI asserts that cause precedes effect. Given two oscillatory timeseries, PSI investigates whether a slight increase/decrease in the oscillatory frequency of the first (i.e. a frequency shift) consistently predicts the same behavior in the second at a fixed delay. If frequency shifts in the two are unrelated, PSI ≈ 0. If frequency shifts in one signal *drive* (i.e. lead) the other, PSI > 0 or PSI < 0, depending on the direction of the interaction. In this way, PSI captures a notion of causality between timeseries. Critically, we also note that PSI is a band-limited metric—PSI is computed in a predefined frequency band where a causal interaction is expected. We refer the reader to the above references for further technical detail.

For sensor-space PSI analysis, broadband data and alpha envelopes for each trial (from t = −8 to t = 0.9 seconds) were padded to 10s, windowed with a Hanning taper and decomposed with Fourier analysis in the delta band (*ft_freqanalysis*, method: mtmfft, foi: [1:0.1:2]). PSI was then computed with *ft_connectivityanalysis* (method: psi, bandwidth: 1, jackknife: yes). PSI values were divided by the jack-knifed standard error of the mean (SEM) before subsequent averaging across electrodes, plotting and statistical analysis.

PSI analysis was also conducted in source space. For this analysis, average filters generated by source fitting broadband timeseries were used to compute voxel-level timeseries for each trial. To simplify computation, each voxel was projected onto its principle eigenvalue before timeseries extraction, and after projection, the source voxel space was downsampled by a factor of 3. Timeseries were then frequency decomposed as in the sensor-space PSI analysis, and PSI was computed for each voxel pair.

Results

Attention engages a frontal source

Averaged, time-locked potentials to each checkerboard stream are shown in Figure 2 for the attended (hit trials only) and unattended conditions. Data are collapsed across stimulus configuration after: 1. conversion to a common domain (cycles elapsed) and 2. interpolation of the 1.5 Hz stream. Averaged signals from two posterior sensor pools are shown for comparison to Gray, Frey et al. (2015), as are delta-filtered (1–2 Hz) versions of the same data. T_0 (T = 0) denotes the initial presentation of the duration deviant, whereas T_1 (T = 1) marks the moment of expectancy violation, where checkerboard rotation is expected but *does not occur* because of the inserted delay. Supplementary Figures 1 and 2 show the data

processed in the same manner—averaged across trials and sensor group—but *not* collapsed across stimulus configuration. Supplementary Figure 3 presents Fourier decomposition of the data in Supplementary Figures 1 and 2. Topographies of power at the fundamental frequency in each case are also shown. By contrast, in Supplementary Figure 4, we compute the power spectra *before* averaging across trials. Taken together, Figure 2 and Supplementary Figures 1–4 demonstrate that, although broadband power is evident in single trials, the averaged, time-locked responses oscillate predominantly at the attended delta frequency (and its harmonics).

Next, we submit the broadband data in Figure 2 to a cluster-based, nonparametric randomization test (Maris and Oostenveld 2007) with factors condition (attended/unattended) and checkerboard hemifield (left/right). As in Figure 2, only hit trials were included in the attended condition for this analysis. Figure 3 displays the significant main effect of attention during the task and is masked by cluster-corrected significance ($p < 0.05$). Supplementary Figure 5 shows the same analysis for the main effect of hemifield and the condition × hemifield interaction. In addition to the broad, significant main effects of attention and hemifield on the stimulation interval ($T < 0$), we also observe a significant main effect of attention at T_1 (see the dashed, black box in Figure 3, *Top Left*). This effect is displayed topographically in Figure 3, *Top Right* by collapsing values across the boxed interval from $T = 0.715$ to $T = 1.17$ cycles elapsed ($t = 550 – 900$ ms). Data from each electrode are masked by significance ($p < 0.05$ for at least five samples on the T_1-interval). Source localization for the attention contrast is shown in Figure 3, *Middle*. A binary mask for this region is generated by thresholding at 3.25×10^{-6}. Nonparametric randomization testing on power values averaged across this mask reveal a significant increase in source power on the T_1-interval during the attended condition relative to the unattended condition ($p < 10^{-4}$; Cohen's paired-sample *d*: 1.24). The mask was also used to extract the source-power time-course during the experiment (shown in Figure 3, *Bottom*). We note that, for the attended condition, there is an apparent increase in source power over baseline during the T_1 interval. To confirm this effect, we again employ a nonparametric randomization test ($p = 0.0078$; Cohen's paired-sample *d*: 0.55). Note that, for this test, baseline is defined as the average source power in the time-matched interval from $T = -0.455$ to $T = 0$.

Supplementary Figure 5 demonstrates that another (albeit weaker) focal source is detected during the T_1-interval. To isolate this source, we mask all data anterior to $Y = -50$ (RAS coordinate system). We then employ a threshold (2.1×10^{-6}) to generate a binary mask and extract average source power values. Randomization testing reveals a significant increase in source power during the T_1-interval for the attended condition with respect to the unattended condition ($p < 10^{-4}$; Cohen's paired-sample *d*: 0.96). We also note a small peak in occipital source power near T_1; however, we hesitate to over-interpret it here.

Frontal activity correlates with performance

In Figure 4, we examine the relationship between electrophysiological activity and behavior. In particular, we investigate gross differences between hit trials (where subjects correctly report the duration deviant) and miss trials (where they do not). Cluster-based, nonparametric statistical testing reveals a significant main effect of performance (hit vs.

miss) during the T_1-interval. However, on the same interval, no significant main effect of hemifield nor performance × hemifield interaction are observed (see Supplementary Figure 6). Again, significance-masked topographies over the T_1-interval are constructed (note the similarity to significance-masked topographies in Figure 3).

Given previous work connecting oscillatory phase and behavior, we define two sensor groups (parietal and frontal) from the topographies in Figure 4, *Top Right*, and we pool together their estimates of delta phase at T_1 as a function of performance (see Methods, Data Analysis, Timeseries Analysis). Circular histograms underlying these mean data are also shown. For all four cases (hit/miss × frontal/parietal), Rayleigh's test of non-uniformity rejects the null hypothesis that the data are uniformly distributed (Rayleigh $z_{hit,frontal} = 18.4$, $p_{hit,frontal} = 3 \times 10^{-11}$; Rayleigh $z_{hit,parietal} = 15.0$, $p_{hit,parietal} = 1.3 \times 10^{-8}$; Rayleigh $z_{miss,frontal} = 10.8$, $p_{miss,frontal} = 5 \times 10^{-6}$; Rayleigh $z_{miss,parietal} = 8.6$, $p_{miss,parietal} = 8.5 \times 10^{-5}$, all uncorrected). These values were submitted to a two-factor (Harrison-Kanji) circular ANOVA with factors performance and sensor group. A significant main effect of sensor group is observed ($\chi^2_{(2,46)} = 96.39$; $p < 10^{-4}$) as is a significant performance × sensor group interaction ($\chi^2_{(1,92)} = 7.74$; $p = 0.005$). No significant main effect of performance is detected ($\chi^2_{(2,46)} = 0.84$; $p = 0.66$). Post-hoc Watson-Williams testing reveals that the interaction term is driven by the parietal sensor group, for which we observe a significant difference in hit/miss mean angles ($F_{(1,44)} = 8.15$; $p = 0.007$, uncorrected). The frontal sensor group shows no such effect ($F_{(1,44)} = 1.47$; $p = 0.23$, uncorrected). However, as the angular values indicate activity suggestive of a dipole (with phase offset π across sensor group), we instead take the angular difference between frontal and parietal sensor groups. In both hit and miss conditions, a one-sample test fails to reject (cannot exclude) that the angular difference across sensor groups is π (in radians: hit 95% CI [2.86,3.41]; miss 95% CI [2.14,3.44]). Thus, the data are overall consistent with the notion that the two sensor groups detect the opposite ends of a dipole whose phase at T_1 does not seem to relate to performance. However, as the analysis in Figure 4, *Top Left* demonstrates, the data do support a relationship between the gross hit/miss trial classification and activity in the T_1 interval, even if only in the strength of this activity (and not its phase).

As before, we source-localize activity on the T_1-interval. In Figure 4, *Middle*, we observe a similar activation pattern as in the attended vs. unattended contrast (Figure 3, *Middle*). Unlike the attended contrast, however, no other focal sources are observed for the performance contrast. Randomization testing on mean power data extracted with a binarized mask of this region (threshold: 0.75×10^{-6}) confirms an increase in source power on the T_1 interval for the hit condition relative to the miss condition ($p = 0.03$; Cohen's paired-sample *d*: 0.39). Time courses for source power are displayed in Figure 4, *Bottom*. Whereas a T_1-interval increase in source power over baseline was previously confirmed for the attended (i.e. hit) condition, the same randomization testing on the miss data fails to support such an effect ($p = 0.88$; Cohen's paired-sample *d*: −0.26).

Frontal delta phase correlates with behavior

For finer-grained analysis relating T_1-interval activity to behavior, we examine hit trials exclusively. Across experimental sessions, average reaction times (in ms) were: 610 (Day 1;

σ = ±80); 630 (Day 2; σ = ±100); and 610 (Day 3; σ = ±100). Average hit rates across experimental session were: 66% (Day 1; σ = ±14%); 64% (Day 2; σ = ±17%); and 65% (Day 3; σ = ±17%). For additional behavioral analysis by experimental session, see Wilson, Gray et al. (2018; especially Figure 3). As shown in Figure 5, *Top Left*, average reaction times (in ms) for each condition were: Left (1.5 Hz): 610 (σ = ±90); Left (1.3 Hz): 610 (σ = ±100); Right (1.5 Hz): 630 (σ = ±90); Right (1.3 Hz): 620 (σ = ±90). A repeated measures ANOVA on the reaction time data reveals a main effect of checkerboard hemifield ($F_{(1,22)}$ = 11.10; p = 0.003), explained by a small decrease in reaction time for the deviants in the left hemifield (in ms: 95% CI [6.7,28.7]). No significant main effect of checkerboard rotation frequency is observed ($F_{(1,22)}$ = 1.43; p = 0.24). Lastly, a checkerboard hemifield × rotation frequency interaction did not reach significance ($F_{(1,22)}$ = 3.87; p = 0.06).

As previous work demonstrates a relationship between reaction time and oscillatory phase (e.g. Lakatos, Karmos et al. 2008), we interrogate our data for any such effect. For this analysis, average delta-phase values at T_1 were pooled across the parietal sensor group (Figure 4, *Top Right*, green electrodes). Trials were binned by delta phase, and average reaction times were computed per bin. Figure 5, *Top Right* shows the result of this analysis. Statistical testing reveals a significant circular-linear correlation, confirming the relationship between delta phase at T_1 and reaction time (ρ = 0.40; p = 5×10^{-7}).

In Figure 5, *Middle*, we plot VEPs evoked by unattended checkerboards as a function of delta phase, which was again estimated with the parietal sensor group (Figure 4, *Top Right*, green electrodes) . VEPs are collapsed across electrodes shown in Figure 5, *Middle*. In all phase bins, we observe a P1 component with latency 85 to 100 ms. In Figure 5, *Bottom Left*, we extract average amplitudes over the P1 interval (shaded in Figure 5, *Middle*) and plot them as a function of binned delta phase. As with the reaction time data, we observe a significant circular-linear correlation between delta phase at unattended checkerboard presentation and average P1 amplitude (ρ = 0.30; p = 2×10^{-4}). We also note that P1 amplitude and reaction time share a similar relationship with delta phase, suggesting that, when delta phase is between $\pi/4$ and $3\pi/4$, both the amplitude of the P1 evoked by the unattended stimulus and the reaction time to the duration deviant are reduced. These two independent measurements therefore suggest that the delta-filtered activity measured at parietal sensors has a *preferred phase* at which task-related performance is optimized relative to non-preferred phases.

Attention modulates ipsilateral alpha power at T_1

During visuospatial attention tasks, covert attention to a lateralized visual stimulus increases posterior alpha power ipsilaterally and decreases it contralaterally. By computing average power topographies over the alpha band (8–14 Hz) from the data in Supplementary Figure 4, we confirm that this pattern is also present in the current data (Figure 6, *Top*). Time-resolved alpha envelope trajectories are shown in Figure 6, *Middle* for attended (hit trials only) and unattended conditions. As with Figure 2, data were collapsed across stimulus configuration by converting from the time domain (in seconds) to the number of checkerboard cycles elapsed. For reference, alpha envelope trajectories before collapse across stimulus configuration are shown in Supplementary Figure 7. Alpha envelopes were also baseline

corrected by high-pass filtering at 1 Hz (see Methods, Data Analysis, Delta Filtering and Alpha Envelopes). The frequency spectra of these envelopes are shown in Supplementary Figures 8 and 9. Together, they demonstrate that the alpha envelopes show in-phase oscillations at the epoching frequency, despite that broadband (1–4 Hz) power is present in individual trials.

Next, we submit the alpha envelope data to non-parametric, cluster-corrected randomization testing as a function of attention. However, given that we are primarily interested in alpha activity *relative to the checkerboard of interest* (i.e. *ipsilateral* or *contralateral* to the epoching checkerboard), we mirror data epoched to the right checkerboard across the x-axis (the sagittal plane) before statistical testing. In effect, this transformation is a mechanism for book-keeping; after mirroring, ipsilateral data in each condition can be extracted from sensors left of midline, regardless of which checkerboard (left or right) was actually attended; similarly, all contralateral data is found in sensors right of midline. Statistical testing is then employed with factors condition (attended/unattended) and mirror (mirrored/not mirrored; i.e. a proxy for left/right).

Figure 6, *Bottom Left* displays the averaged difference between the attended (hit trials only) and unattended conditions masked by cluster-corrected significance ($p < 0.05$). Throughout the entire time interval tested, no significant main effect of mirror nor significant condition × mirror interaction were observed (data not shown as significance masking covers the entirety of the plotted interval). We observe a significant main effect of attention on the T_1-interval, and we again construct significance-masked, topographic representations for reference, where electrodes are shown if they retained significance for at least sixteen time points in the T_1-interval. The topographies demonstrate that the significant decrease in alpha power during the T_1-interval can be localized to *ipsilateral* sensors (i.e. left sensors post-mirroring). Source localization for this effect is plotted in Figure 6, *Bottom Right*. As an additional control, we take the broadband, time-locked data in Figure 2, compute its alpha envelope directly and deploy the same statistical approach; for this analysis, no statistically significant differences were detected between the attended and unattended conditions during the entire interval in Figure 2, including the T_1-interval.

As with the broadband data, we next examine alpha envelopes as a function of task performance (hit vs. miss) by employing the same omnibus nonparametric statistical strategy. No significant effect of task performance is found during the entire interval tested, nor is any significant main effect of mirroring nor any performance × mirror interaction. However, given that we have identified a significant, attention-related effect during the T_1-interval for ipsilateral electrodes, we specifically test for a performance-related effect averaged across the T_1-interval in the significant electrodes in Figure 6, *Bottom Middle* by employing an FDR-corrected, non-parametric randomization strategy. Whereas a main effect of mirroring and a performance × mirror interaction are not significant ($p = 0.92$ and $p = 0.43$ respectively, FDR-corrected), we observe a significant main effect of performance ($p = 0.03$, FDR-corrected), indicating a significant decrease in alpha power measured at these sensors in the hit condition with respect to the miss condition. Thus, although the omnibus strategy does not return significant results, a specific test for the effect of interest does.

Frontal delta activity and ipsilateral alpha power are coupled

Two neural sources of interest have thus been identified. One, a frontocentral generator, oscillates at the attended frequency and cyclically correlates with task performance; the other, an ipsilateral, posterior generator, shows fluctuations in alpha power at the rhythm of the attended stimulus. Figure 7 investigates their interaction and its relation to task performance. In particular, Figure 7, *Top* shows the average (high-pass filtered) magnitude of the ipsilateral alpha envelope as a function of frontal delta phase for hit and miss conditions. The ipsilateral alpha envelope is taken from significant sensors in Figure 6, *Bottom Middle*, whereas the frontal delta phase is computed at the significant parietal sensors in Figure 4, *Top Right*. Both hits and misses show significant circular-linear correlation between alpha envelope magnitude and delta phase (hits: $\rho = 0.28$, $p = 6.5 \times 10^{-4}$; misses: $\rho = 0.25$, $p = 0.003$). To detect any differences in alpha-delta circular-linear correlation as a function of performance, we compute ρ in hit and miss conditions for each participant separately. These values are shown via raincloud plot (Allen, Poggiali et al. 2018) in Figure 7, *Middle*, where it appears that ρ is increased for hits relative to misses. Indeed, a non-parametric randomization test is consistent with this assertion ($p = 0.03$; Cohen's paired-sample *d*: 0.40). Note that the choice to employ parietal sensors to estimate delta phase is arbitrary. The significant frontal sensors in Figure 4, *Top Right* could be employed instead. In this case, we still observe significant circular-linear correlations between alpha envelope magnitude and delta phase in both conditions (hits: $\rho = 0.26$, $p = 2.1 \times 10^{-3}$; misses: $\rho = 0.37$, $p = 4.7 \times 10^{-6}$). However, in this analysis, randomization testing does not detect a difference in ρ between hit and miss conditions ($p = 0.85$; Cohen's paired-sample d: −0.23; see also Supplementary Figure 10).

We next examine the phase-slope index (PSI) between frontal delta activity and ipsilateral alpha power (see Methods, Data Analysis, Phase-Slope Index). PSI data are initially computed for each electrode pair and then collapsed over posterior, ipsilateral electrodes (i.e. the significant sensors in Figure 6, *Bottom Middle*). Figure 7, *Middle* shows a contrast between hit and miss conditions. As a result, electrodes with PSI > 0 have delta activity that drives ipsilateral, posterior alpha power more strongly in the hit condition than in the miss condition. We again submit this data to a nonparametric, cluster-corrected randomization test, and in the right topography of Figure 7, *Middle*, we mask the contrast by statistical significance ($p < 0.05$). We observe that PSI between frontal delta activity and posterior, ipsilateral alpha power is increased in hits relative to misses. In Figure 7, *Bottom*, we extract individual PSI values, averaged across the significant sensors in Figure 7, *Middle.* Again, these data points are shown in raincloud format, and we confirm the same increase in PSI for hits over misses ($p = 0.003$ by randomization testing; Cohen's paired-sample *d*: 0.67). For each condition, we also perform an uncorrected Wilcoxon sign rank test, and observe that, during the hit condition, we can exclude that the PSI values have a median of zero ($p = 0.02$; $\mu_{obs} = 0.1$), whereas, in the miss condition, we cannot ($p = 0.83$; $\mu_{obs} = -0.09$).

As a convergent line of evidence, we repeat the same PSI analysis in source space. As in the topographic analysis, PSI values are collapsed across ipsilateral, posterior sites before plotting; however, in this case, the voxel mask used for collapse is generated by thresholding the data in Figure 6, *Bottom Right* at 2.85×10^{-4} au. Figure 7, *Bottom Right* again shows a

contrast between hit and miss trials. PSI values in the colored frontocentral region are thus, on average, increased in hits relative to misses ($p = 0.002$ by randomization testing; Cohen's paired-sample d: 0.67). We also observe that average PSI at frontal voxels is positive during hit trials ($p = 0.05$ by Wilcoxon sign rank test; $\mu_{obs} = 0.09$), whereas we find PSI to be negative during miss trials ($p = 0.02$ by Wilcoxon sign rank test; $\mu_{obs} = -0.08$). Finally, we note that Supplementary Figure 10 performs a complementary analysis; instead of collapsing across posterior, ipsilateral voxels prior to plotting, data are collapsed over frontocentral voxels. The mask employed for this analysis is drawn from Figure 3, *Middle* by thresholding at 3.25×10^{-6} au, and again, a hit vs. miss contrast is shown. After mirroring, we observe a posterior, ipsilateral region (i.e. a left-lateralized region post-mirror) where PSI appears to be greater in hit trials than in miss trials. However, the hit vs. miss effect in this region does not reach significance ($p = 0.18$ by randomization testing; Cohen's paired-sample d: 0.2).

Discussion

The Spatial CTET elicits frontal entrainment to the frequency of the attended visual stream

We here demonstrate that broadband EEG activity during the Spatial CTET oscillates at the frequency of the attended checkerboard stream. Two possible mechanisms might underlie this observation: stimulus-evoked activity and neural entrainment. We note that: 1. VEPs generally returns to baseline around 500 ms after stimulus presentation (Di Russo, Teder-Sälejärvi et al. 2003); and 2. VEPs are necessarily elicited by a stimulus—without stimulus presentation, no evoked activity is possible by definition. Therefore, attention-related activity the moment of expectancy violation (T_1) cannot be stimulus-evoked as it occurs at least 667 ms after onset of the deviant at T_0 and, moreover, no new stimulus is presented at T_1. Yet, we note a frontal source whose activity during the T_1 interval is modulated by attention and task performance.

The alternative explanation, entrainment, typically requires the pre-existence of an oscillator that *becomes entrained* to rhythmic input from another oscillator. Although this is difficult to establish with extracranial methods like EEG, the phenomena has been well-studied with a variety of intracranial methods in both humans and non-human primates (e.g. Lakatos, Karmos et al. 2008, Besle, Schevon et al. 2011, Lakatos, Barczak et al. 2016). This body of work also demonstrates several effects secondary to entrainment, including cyclic modulations of reaction time and evoked activity. Likewise, we observe that the delta phase of the frontal source correlates with both reaction times and VEPs evoked by the unattended checkerboards.

Although we cannot here demonstrate local, pre-existing oscillators that become entrained during the Spatial CTET, our results are inconsistent with a purely evoked account and reproduce previous findings associated with entrainment. We therefore conclude that, in addition to the VEPs evoked by checkerboard presentation, the Spatial CTET elicits frequency-specific frontal entrainment to the attended checkerboard stream.

As brief aside, we also note that an occipital source is active during the T_1 interval as a function of attention. Although right-lateralized, this distribution is bilateral, consistent with our prior claim that the Spatial CTET elicits bilateral, posterior entrainment (Gray, Frey et

al. 2015). The rightward lateralization is also curious, however, as it is thought that a right-lateralized network of frontal and parietal regions coordinates spatial attention, including the deployment of alpha oscillations (e.g. Capotosto, Babiloni et al. 2009). However, given the scope of this report, no definitive conclusions can be made regarding this observation, and we hesitate to speculate further at this time.

Ipsilateral alpha power is coupled to the phase of entrained delta oscillations

We observe that alpha envelopes also oscillate at the frequency of the epoching checkerboard stream. While suggestive, VEP components are known to have spectral content in the alpha band; as such, alpha power oscillations at the stimulation frequency might reflect an artifact of filtered, time-locked VEPs. As before, we focus on the T_1 interval, which is unlikely to reflect stimulus evoked activity, and we observe an attention-related decrease in ipsilateral alpha power at the moment of expectancy violation. Additional statistical analysis moderately supports the claim that this effect is also related to task performance (hit vs. miss).

Our comodulograms analysis shows that frontal delta phase and ipsilateral alpha power are correlated and that this correlation is increased during hits as compared to misses. Yet, we note that this correlation is not detected if the significant frontal sensors in Figure 4, *Top Right* are used to estimate frontal delta phase. There is therefore mixed evidence that the *interaction* between these two sources correlates with task performance. However, even if it were, a performance-related increase in ρ may not be driven by any mechanistic interaction between the two sources at all. Instead, it might be that both are independently more strongly coupled to the attended frequency in hits (vs. misses). In that case, the two need not interact directly (nor at all) to see an apparent increase in correlation between their activities (i.e. the common-driver fallacy).

PSI analysis helps to tease these possibilities apart, as it examines how frequency shifts in the first source predict those in the second at some fixed delay, which is a much stronger and more specific claim than a simple circular-linear correlation. We observe increased PSI from frontal delta activity to ipsilateral alpha power in hits vs. misses. Statistical testing also suggests that PSI is positive in hit trials (frontal delta activity *drives* the ipsilateral alpha envelope), whereas PSI cannot be distinguished from 0 in misses. This observation is consistent with the notion that the *causal structure* of this alpha-delta interaction correlates with task performance. Two independent source-space analyses support the same conclusion; however, we do note that, given the source-localization accuracy of EEG, further intracranial work will be necessary to confirm that the entrained frontal source is the same source that drives the ipsilateral alpha envelope. Nonetheless, given multiple, independent lines of convergent evidence, we contend that the most likely explanation for our data is that frontal delta and ipsilateral alpha activity are phase-amplitude coupled. In particular, we assert that the entrained frontal source causally drives ipsilateral alpha activity in the delta band.

However, explicitly testing this purported causal structure will be necessary to validate or contradict these interpretations. In the meantime, we note that prior empirical work suggests a causal role for frontoparietal regions in the control of posterior alpha activity, underscoring

the plausibility of our analysis and interpretation (Capotosto, Babiloni et al. 2009, Marshall, O'Shea et al. 2015, Helfrich, Huang et al. 2017).

Entrainment as a tool to organize macroscale networks

The oscillation of alpha power at an attended delta frequency has been previously shown in other experimental settings (Gomez-Ramirez, Kelly et al. 2011, Wostmann, Herrmann et al. 2016). Another line of work suggests that alpha and delta activities are generally anti-correlated and represent two distinct functional states or attentional strategies (Lakatos, Barczak et al. 2016, Henry, Herrmann et al. 2017). However, these studies employed auditory and mixed audiovisual stimuli; as such, whether (and how) they generalize to the visuospatial domain is unclear, and any comparison should be treated with caution. That said, our findings generally support that alpha power and delta activity work together to shape a single attentional strategy, although it is not clear that the two hypotheses are mutually exclusive.

Our analyses extend the understanding of these individual phenomena (and their interaction) in a few interesting and important ways. To start, we note that convergent empirical (Worden, Foxe et al. 2000, Kelly, Lalor et al. 2006, Hanslmayr, Aslan et al. 2007, Romei, Gross et al. 2010, Snyder and Foxe 2010, Banerjee, Snyder et al. 2011, Handel, Haarmeier et al. 2011) and theoretical (Ching, Cimenser et al. 2010, Vijayan and Kopell 2012) evidence supports the hypothesis that increased occipital alpha power inhibits visual processing as a function of selective attention (Foxe and Snyder 2011). In light of this body of work, our finding that ipsilateral alpha power is coupled to the temporal structure of the attended environment is not surprising. After all, the evolutionary imperative is not necessarily to suppress information processing *per se*; rather, it might be to suppress processing *at the appropriate time*.

One strategy for organizing the temporal structure of alpha power is to couple its time-course to a rhythm of interest. On this point, our data are suggestive of an underlying mechanism. It appears that frontocentral regions entrain to the attended environmental input and that ipsilateral alpha power is driven by this frontal delta activity. Although previous work has focused predominantly on entrainment in sensory cortices (e.g. Lakatos, Karmos et al. 2008, Besle, Schevon et al. 2011, Gomez-Ramirez, Kelly et al. 2011, Lakatos, Barczak et al. 2016, Wostmann, Herrmann et al. 2016), our finding of strong, directed frontocentral entrainment suggests that it may play a previously underappreciated role in coordinating network-level interactions across distributed neural systems.

Alpha power as a temporal filter

There continues to be healthy discourse about whether visuospatial attention primarily serves to suppress processing of unattended inputs through alpha synchrony (Rihs, Michel et al. 2007) or facilitate processing of attended inputs by alpha desynchrony (Rohenkohl and Nobre 2011, Foster and Awh 2018). In principle, one or both of these mechanisms may contribute to alpha lateralization in visuospatial attention tasks (e.g. Worden, Foxe et al. 2000, Thut, Nietzel et al. 2006, Gray, Frey et al. 2015). While we also observe alpha lateralization, it is not the case that this alpha power is tonically deployed. Rather, ipsilateral

alpha power oscillates at the frequency of the attended stimulus, and at the moment that an event is expected in the attended hemifield, ipsilateral alpha power is maximally suppressed. To the extent that changes in alpha power are a proxy for suppression/facilitation of processing, one might infer that we observe *both* effects in a counterposed (i.e. oscillatory) fashion. In any case, it appears that the role of alpha (suppression vs. facilitation vs. *both*) is flexible and depends on, among other things, the temporal constraints of the task.

Considered in the *alpha as inhibition* framework, we suggest that coupling alpha power to an attended environmental rhythm may serve two related functions. Firstly, by cycling alpha power at the attended frequency, the strength of inhibition is dynamically modulated, suggesting that sampling of the unattended side of space might occur regularly, despite that subjects are cued to attend only to one visual hemifield. Thus, frontal delta entrainment might rhythmically release ipsilateral cortex from inhibition by increased alpha power. Teleologically, this may be an adaptive advantage—it may be beneficial for an organism to periodically sample unattended environmental inputs as a method of updating or confirming predictions. Secondly, the unattended stream is sampled at ecologically important moments. It may be that sampling the unattended visual input at the relevant moments also serves to gather additional information about inputs in the environment that are correlated with attended input and, conversely, to suppress inputs whose temporal structures are not—i.e. alpha power might be deployed as a *temporal filter*.

Supporting the ecologic validity of that notion, we note that attention-related changes in ipsilateral alpha power persist despite strong, concurrent stimulation in the unattended visual field, suggesting that not all generators of posterior alpha activity are desynchronized by incoming inputs and/or that the brain has intrinsic mechanisms to maintain alpha generator synchrony despite direct stimulation. Our data therefore bolster the claim that modulations in lateralized alpha power are functionally significant in real-world environments, where constant visual input might be predicted to disrupt ongoing alpha activity.

Other authors have proposed, however, that alpha-band physiology is likely more complex than the *alpha as inhibition* framework may suggest. In particular, alpha *phase* has been suggested to play a role in perception, action and memory that is not solely inhibitory (Palva and Palva 2007). These viewpoints need not be exclusionary—modulations in both alpha phase and alpha power may play complimentary roles in neural computation (e.g. Gips, van der Eerden et al. 2016). It is also conceivable that the alpha activity engaged by lateralized spatial attention tasks may be qualitatively different than the alpha observed in non-lateralized tasks (Foster and Awh 2018). To that end, we note that great care must be taken in generalizing the present findings to other contexts. Unfortunately, the current experimental paradigm was not designed to test these hypotheses; as such, insight from the current work on these points is limited.

Interactions between temporal and spatial attention

Regardless, one reasonable interpretation of lateralized alpha power during visuospatial attention tasks is that it is a mechanism of spatial attention. Entrainment, on the other hand, can be interpreted a mechanism of temporal attention. Typically, these constructs (spatial and temporal attention) are treated independently. However, we here observe an interaction

between them wherein a mechanism of spatial attention appears to be modulated by a mechanism of temporal attention. A recent study by Wostmann, Herrmann et al. (2016) demonstrates a similar outcome. In their case, however, changes in alpha lateralization are driven by differences in both ipsilateral and contralateral alpha activity.

In the current experiment, we observe that stimulation-independent changes in alpha lateralization are primarily found ipsilaterally (Figure 6). One explanation for this seeming-contradiction is a difference in task design. In their study, Wostmann, Herrmann et al. (2016) employ two auditory inputs, but both streams are temporally coordinated with one another. In our study, the competing streams are temporally uncorrelated. Thus, when streams compete directly, it may be that both increased ipsilateral alpha and decreased contralateral alpha power are necessary to resolve ongoing competition between stimuli. Instead, in our case, it may be that frequency-specific delta entrainment of frontocentral regions is enough to resolve this competition. Alpha oscillations may thus be freed to act as a temporal filter on the unattended inputs.

In support of this idea, a related study by Rohenkohl and Nobre (2011) suggests a similar conclusion. In their study, an attended object was presented, and its temporal predictability differed between conditions; critically, no competing unattended object was presented, and the target appeared in only one hemifield. As compared to the non-predictable condition, the predictable condition showed decreased bilateral occipital alpha power in the 200 ms preceding expected stimulus presentation, suggesting that both ipsilateral and contralateral alpha oscillations were desynchronized in preparation for stimulus processing. In effect, these investigations suggest that temporal modulation of alpha activity can act also act as a mechanism of temporal attention and, consequently, that spatial and temporal attention might (in some circumstances) share underlying neural mechanisms.

Mechanisms of alpha-delta coupling

The mechanistic underpinnings of the observed alpha-delta coupling are also unclear, and insight from the analysis employed here is unfortunately limited. However, it is known that white matter tracts that run directly between frontal and posterior regions are correlated to alpha lateralization during spatial attention tasks (Marshall, Bergmann et al. 2015). In the current work, it may therefore be that visual information is propagated to frontocentral areas, after which it is relayed posteriorly by these fibers to modulate alpha lateralization. Given the putative role of subcortical structures like the pulvinar in coordinating distributed visuocortical synchrony (Saalmann and Kastner 2011, Saalmann, Pinsk et al. 2012), we also expect that subcortical structures might contribute to modulations in ipsilateral alpha activity.

One other possibility is that frontal activity and ipsilateral alpha power both reflect input from a common driver in addition to their putative interaction. For instance, both areas may receive input regarding the attended rhythm from the contralateral visual cortex to which it is directly presented. Frontal regions might receive this input in a bottom-up fashion, whereas ipsilateral cortex might receive its input via callosal fibers. As previous work suggests that alpha activity is generated by complex thalamocortical and corticocortical interactions involving deep layers of cortex in particular (Lopes da Silva, Vos et al. 1980, Bollimunta,

Chen et al. 2008, Bollimunta, Mo et al. 2011), it would be particularly interesting to understand how callosal fibers may interact with alpha generative mechanisms.

A separate line of evidence suggests that callosal inputs synapse directly on neurons in deep cortical layers (Karayannis, Huerta-Ocampo et al. 2007) and that stimulation of interhemispheric fibers in rat somatosensory cortex results in layer-specific inhibition in the distal apical dendrites of layer 5 pyramidal neurons (Palmer, Schulz et al. 2012). These two lines of evidence suggest that alpha-delta coupling might be accomplished by convergent inputs to deep layers of ipsilateral cortex. And, as visual-processing-associated gamma oscillations found in granular and superficial cortical layers have been observed to be anti-correlated with alpha in deep layers (Spaak, Bonnefond et al. 2012), the notion that interhemispheric inputs may reduce ongoing alpha oscillations and increase visual processing indeed seems reasonable. Further work will be necessary to tease these non-exclusive conceptual models apart.

Conclusion

The findings presented here add to our understanding of entrainment, alpha oscillations and their interaction during attention. These data also support one answer to a critical, outstanding question in modern cognitive neuroscience: how is it that distributed neural regions are bound into macroscale, functional neural networks? One potential mechanism here demonstrated is through rhythmic entrainment, synchronization and cross-frequency interactions. We believe that continued investigation of oscillatory mechanisms will be of great importance in building an understanding of the physiology of attention—and the brain as a whole.

Supplementary Material

Refer to Web version on PubMed Central for supplementary material.

Acknowledgements:

This work was supported in part by a grant from the Pepsi Corporation (Pepsi-Co) to Dr. Foxe (PEP 1323). The authors' investigation of neural oscillations and attention was also supported by the National Science Foundation (NSF BCS1228595). Drs. Wilson and Foxe thank Sydney Jacobs and Haleigh Smith for help with data collection. Dr. Wilson received partial support from a National Institute of General Medical Sciences (NIGMS) Medical Scientist Training Program Grant (T32 GM007288). The authors declare no competing financial interests that would in any way bias the results reported herein.

References

Allen M, Poggiali D, Whitaker K, Marshall TR and Kievit R (2018). "Raincloud plots: a multi-platform tool for robust data visualization." PeerJ Preprints 6: e27137v27131.

Banerjee S, Snyder AC, Molholm S and Foxe JJ (2011). "Oscillatory alpha-band mechanisms and the deployment of spatial attention to anticipated auditory and visual target locations: supramodal or sensory-specific control mechanisms?" J Neurosci 31(27): 9923–9932. [PubMed: 21734284]

Besle J, Schevon CA, Mehta AD, Lakatos P, Goodman RR, McKhann GM, Emerson RG and Schroeder CE (2011). "Tuning of the human neocortex to the temporal dynamics of attended events." J Neurosci 31(9): 3176–3185. [PubMed: 21368029]

Bollimunta A, Chen Y, Schroeder CE and Ding M (2008). "Neuronal mechanisms of cortical alpha oscillations in awake-behaving macaques." J Neurosci 28(40): 9976–9988. [PubMed: 18829955]

Bollimunta A, Mo J, Schroeder CE and Ding M (2011). "Neuronal mechanisms and attentional modulation of corticothalamic alpha oscillations." J Neurosci 31(13): 4935–4943. [PubMed: 21451032]

Capotosto P, Babiloni C, Romani GL and Corbetta M (2009). "Frontoparietal cortex controls spatial attention through modulation of anticipatory alpha rhythms." J Neurosci 29(18): 5863–5872. [PubMed: 19420253]

Ching S, Cimenser A, Purdon PL, Brown EN and Kopell NJ (2010). "Thalamocortical model for a propofol-induced alpha-rhythm associated with loss of consciousness." Proc Natl Acad Sci U S A 107(52): 22665–22670. [PubMed: 21149695]

Correa A, Lupianez J, Madrid E and Tudela P (2006). "Temporal attention enhances early visual processing: a review and new evidence from event-related potentials." Brain Res 1076(1): 116–128. [PubMed: 16516173]

Delorme A and Makeig S (2004). "EEGLAB: an open source toolbox for analysis of single-trial EEG dynamics including independent component analysis." J Neurosci Methods 134(1): 9–21. [PubMed: 15102499]

Di Russo F, Martínez A, Sereno MI, Pitzalis S and Hillyard SA (2002). "Cortical sources of the early components of the visual evoked potential." Human Brain Mapping 15(2): 95–111. [PubMed: 11835601]

Di Russo F, Teder-Sälejärvi WA and Hillyard SA (2003). Steady-State VEP and Attentional Visual Processing The cognitive electrophysiology of mind and brain. Zani A and Proverbio AM, Academic press: 257–272.

Foster JJ and Awh E (2018). "The role of alpha oscillations in spatial attention: limited evidence for a suppression account." Curr Opin Psychol 29: 34–40. [PubMed: 30472541]

Foxe JJ, Doniger GM and Javitt DC (2001). "Early visual processing deficits in schizophrenia: impaired P1 generation revealed by high-density electrical mapping." Neuroreport 12(17): 3815–3820. [PubMed: 11726801]

Foxe JJ, Simpson GV and Ahlfors SP (1998). "Parieto-occipital approximately 10 Hz activity reflects anticipatory state of visual attention mechanisms." Neuroreport 9(17): 3929–3933. [PubMed: 9875731]

Foxe JJ and Snyder AC (2011). "The Role of Alpha-Band Brain Oscillations as a Sensory Suppression Mechanism during Selective Attention." Front Psychol 2: 154. [PubMed: 21779269]

Gips B, van der Eerden JP and Jensen O (2016). "A biologically plausible mechanism for neuronal coding organized by the phase of alpha oscillations." Eur J Neurosci 44(4): 2147–2161. [PubMed: 27320148]

Gomez-Ramirez M, Kelly SP, Molholm S, Sehatpour P, Schwartz TH and Foxe JJ (2011). "Oscillatory sensory selection mechanisms during intersensory attention to rhythmic auditory and visual inputs: a human electrocorticographic investigation." The Journal of Neuroscience 31(50): 18556–18567. [PubMed: 22171054]

Gonzalez CMG, Clark VP, Fan S, Luck SJ and Hillyard SA (1994). "Sources of attention-sensitive visual event-related potentials." Brain Topography 7(1): 41–51. [PubMed: 7803199]

Gray MJ, Frey H-P, Wilson TJ and Foxe JJ (2015). "Oscillatory recruitment of bilateral visual cortex during spatial attention to competing rhythmic inputs." The Journal of Neuroscience 35(14).

Handel BF, Haarmeier T and Jensen O (2011). "Alpha oscillations correlate with the successful inhibition of unattended stimuli." J Cogn Neurosci 23(9): 2494–2502. [PubMed: 20681750]

Hanslmayr S, Aslan A, Staudigl T, Klimesch W, Herrmann CS and Bauml KH (2007). "Prestimulus oscillations predict visual perception performance between and within subjects." Neuroimage 37(4): 1465–1473. [PubMed: 17706433]

Helfrich RF, Huang M, Wilson G and Knight RT (2017). "Prefrontal cortex modulates posterior alpha oscillations during top-down guided visual perception." Proceedings of the National Academy of Sciences 114(35): 9457–9462.

Henry MJ, Herrmann B, Kunke D and Obleser J (2017). "Aging affects the balance of neural entrainment and top-down neural modulation in the listening brain." Nature Communications 8: 15801.

Holmes CJ, Hoge R, Collins L, Woods R, Toga AW and Evans AC (1998). “Enhancement of MR images using registration for signal averaging.” J Comput Assist Tomogr 22(2): 324–333. [PubMed: 9530404]

Jensen O and Mazaheri A (2010). “Shaping functional architecture by oscillatory alpha activity: gating by inhibition.” Front Hum Neurosci 4: 186. [PubMed: 21119777]

Jiang H, Bahramisharif A, van Gerven MAJ and Jensen O (2015). “Measuring directionality between neuronal oscillations of different frequencies.” NeuroImage 118: 359–367. [PubMed: 26025291]

Karayannis T, Huerta-Ocampo I and Capogna M (2007). “GABAergic and pyramidal neurons of deep cortical layers directly receive and differently integrate callosal input.” Cereb Cortex 17(5): 1213–1226. [PubMed: 16829551]

Keitel C, Thut G and Gross J (2017). “Visual cortex responses reflect temporal structure of continuous quasi-rhythmic sensory stimulation.” Neuroimage 146: 58–70. [PubMed: 27867090]

Kelly SP, Lalor EC, Reilly RB and Foxe JJ (2006). “Increases in alpha oscillatory power reflect an active retinotopic mechanism for distracter suppression during sustained visuospatial attention.” J Neurophysiol 95(6): 3844–3851. [PubMed: 16571739]

Lakatos P, Barczak A, Neymotin SA, McGinnis T, Ross D, Javitt DC and O’Connell MN (2016). “Global dynamics of selective attention and its lapses in primary auditory cortex.” Nat Neurosci 19(12): 1707–1717. [PubMed: 27618311]

Lakatos P, Karmos G, Mehta AD, Ulbert I and Schroeder CE (2008). “Entrainment of neuronal oscillations as a mechanism of attentional selection.” Science 320(5872): 110–113. [PubMed: 18388295]

Lee TW, Girolami M and Sejnowski TJ (1999). “Independent component analysis using an extended infomax algorithm for mixed subgaussian and supergaussian sources.” Neural Comput 11(2): 417–441. [PubMed: 9950738]

Lopes da Silva FH, Vos JE, Mooibroek J and Van Rotterdam A (1980). “Relative contributions of intracortical and thalamo-cortical processes in the generation of alpha rhythms, revealed by partial coherence analysis.” Electroencephalogr Clin Neurophysiol 50(5–6): 449–456. [PubMed: 6160987]

Maris E and Oostenveld R (2007). “Nonparametric statistical testing of EEG- and MEG-data.” J Neurosci Methods 164(1): 177–190. [PubMed: 17517438]

Marshall TR, Bergmann TO and Jensen O (2015). “Frontoparietal Structural Connectivity Mediates the Top-Down Control of Neuronal Synchronization Associated with Selective Attention.” PLoS Biol 13(10): e1002272. [PubMed: 26441286]

Marshall TR, O’Shea J, Jensen O and Bergmann TO (2015). “Frontal eye fields control attentional modulation of alpha and gamma oscillations in contralateral occipitoparietal cortex.” J Neurosci 35(4): 1638–1647. [PubMed: 25632139]

Nolan H, Whelan R and Reilly RB (2010). “FASTER: Fully Automated Statistical Thresholding for EEG artifact Rejection.” J Neurosci Methods 192(1): 152–162. [PubMed: 20654646]

Nolte G, Ziehe A, Nikulin VV, Schlögl A, Krämer N, Brismar T and Müller K-R (2008). “Robustly Estimating the Flow Direction of Information in Complex Physical Systems.” Physical Review Letters 100(23): 234101. [PubMed: 18643502]

Oostenveld R, Fries P, Maris E and Schoffelen JM (2011). “FieldTrip: Open source software for advanced analysis of MEG, EEG, and invasive electrophysiological data.” Comput Intell Neurosci 2011: 156869. [PubMed: 21253357]

Oostenveld R, Stegeman DF, Praamstra P and van Oosterom A (2003). “Brain symmetry and topographic analysis of lateralized event-related potentials.” Clin Neurophysiol 114(7): 1194–1202. [PubMed: 12842715]

Palmer LM, Schulz JM, Murphy SC, Ledergerber D, Murayama M and Larkum ME (2012). “The cellular basis of GABA(B)-mediated interhemispheric inhibition.” Science 335(6071): 989–993. [PubMed: 22363012]

Palva S and Palva JM (2007). “New vistas for alpha-frequency band oscillations.” Trends Neurosci 30(4): 150–158. [PubMed: 17307258]

Pascual-Marqui RD (2007). “Discrete, 3D distributed, linear imaging methods of electric neuronal activity. Part 1: exact, zero error localization.” arXiv preprint arXiv:0710.3341.

Rihs TA, Michel CM and Thut G (2007). “Mechanisms of selective inhibition in visual spatial attention are indexed by alpha-band EEG synchronization.” Eur J Neurosci 25(2): 603–610. [PubMed: 17284203]

Rohenkohl G and Nobre AC (2011). “Alpha Oscillations Related to Anticipatory Attention Follow Temporal Expectations.” J Neurosci 31(40): 14076–14084. [PubMed: 21976492]

Romei V, Gross J and Thut G (2010). “On the role of prestimulus alpha rhythms over occipito-parietal areas in visual input regulation: correlation or causation?” J Neurosci 30(25): 8692–8697. [PubMed: 20573914]

Saalmann Yuri B. and Kastner S (2011). “Cognitive and Perceptual Functions of the Visual Thalamus.” Neuron 71(2): 209–223. [PubMed: 21791281]

Saalmann YB, Pinsk MA, Wang L, Li X and Kastner S (2012). “The pulvinar regulates information transmission between cortical areas based on attention demands.” Science 337(6095): 753–756. [PubMed: 22879517]

Serences JT, Schwarzbach J, Courtney SM, Golay X and Yantis S (2004). “Control of object-based attention in human cortex.” Cereb Cortex 14(12): 1346–1357. [PubMed: 15166105]

Snyder AC and Foxe JJ (2010). “Anticipatory attentional suppression of visual features indexed by oscillatory alpha-band power increases: a high-density electrical mapping study.” J Neurosci 30(11): 4024–4032. [PubMed: 20237273]

Spaak E, Bonnefond M, Maier A, Leopold DA and Jensen O (2012). “Layer-specific entrainment of gamma-band neural activity by the alpha rhythm in monkey visual cortex.” Curr Biol 22(24): 2313–2318. [PubMed: 23159599]

Thut G, Nietzel A, Brandt SA and Pascual-Leone A (2006). “Alpha-band electroencephalographic activity over occipital cortex indexes visuospatial attention bias and predicts visual target detection.” J Neurosci 26(37): 9494–9502. [PubMed: 16971533]

Vijayan S and Kopell NJ (2012). “Thalamic model of awake alpha oscillations and implications for stimulus processing.” Proc Natl Acad Sci U S A 109(45): 18553–18558. [PubMed: 23054840]

Wilson TJ, Gray MJ, Van Klinken JW, Kaczmarczyk M and Foxe JJ (2018). “Macronutrient composition of a morning meal and the maintenance of attention throughout the morning.” Nutr Neurosci 21(10): 729–743. [PubMed: 28714768]

Winkler I, Haufe S and Tangermann M (2011). “Automatic classification of artifactual ICA-components for artifact removal in EEG signals.” Behav Brain Funct 7: 30. [PubMed: 21810266]

Worden MS, Foxe JJ, Wang N and Simpson GV (2000). “Anticipatory biasing of visuospatial attention indexed by retinotopically specific alpha-band electroencephalography increases over occipital cortex.” J Neurosci 20(6): Rc63. [PubMed: 10704517]

Wostmann M, Herrmann B, Maess B and Obleser J (2016). “Spatiotemporal dynamics of auditory attention synchronize with speech.” Proc Natl Acad Sci U S A.

Zoefel B, Ten Oever S and Sack AT (2018). “The Involvement of Endogenous Neural Oscillations in the Processing of Rhythmic Input: More Than a Regular Repetition of Evoked Neural Responses.” Front Neurosci 12: 95. [PubMed: 29563860]

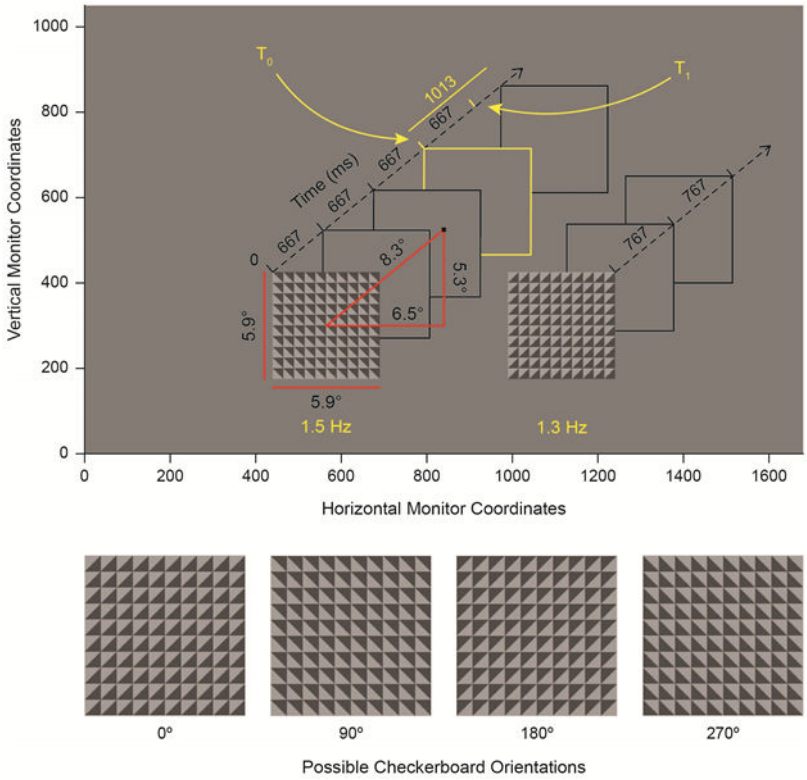

Figure 1:

The Spatial CTET. *Top*: Task layout presented in monitor coordinates. Two checkerboards are presented along with a central, black fixation point. All other items (axes, boxes, angular measurements, etc.) are presented to the reader to illustrate task structure but are not presented during the task. The left-fast stimulus configuration (left checkerboard stream at 1.5 Hz; right at 1.3 Hz) is shown. Gray (and yellow) boxes denote the moments at which new orientations of each checkerboard are presented. Subjects covertly attend one checkerboard stream (left or right) for the duration of a block (~3-4 minutes) and report the appearance of infrequent duration deviants (shown in yellow) via mouse click. The duration deviant is presented at T_0 and exceeds the standard duration at T_1. Both of these times are noted by yellow tick marks on the time axis. Restated, T_1 denotes the moment of expectancy violation, where another checkerboard is expected *but does not occur* because of the inserted delay. Duration deviants appear independently in both checkerboard streams. *Bottom*: The four possible checkerboard orientations.

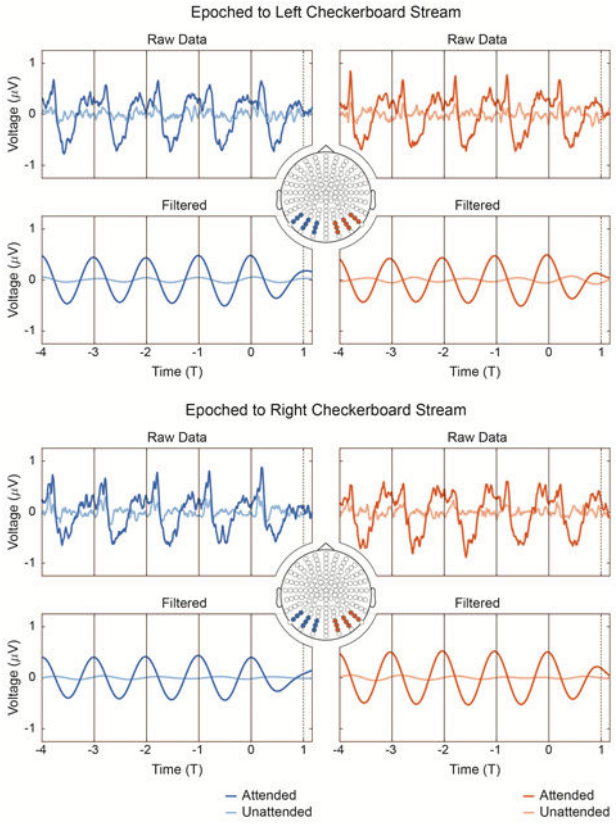

Figure 2:

Evoked potentials, collapsed across stimulus configuration. To collapse across 1.3 and 1.5 Hz stimulus streams, the timescale in each case is converted from seconds to *cycles elapsed* (T) by multiplying each timepoint by the stimulation frequency (e.g. for the 1.5 Hz stream, t = 0.666 s maps to T = (0.666 s)*(1.5 Hz) = 1). In both the 1.3 and 1.5 Hz cases, the dashed line at T_1 (T = 1) indicates the moment at which the next checkerboard rotation is expected but *does not* occur, whereas the solid black vertical lines indicate actual checkerboard rotations. After timescale conversion to this shared domain, the 1.5 Hz stream is interpolated (resampled) to match sampling in the 1.3 Hz stream; the streams are subsequently collapsed (see Methods, Data Analysis, Timeseries Analysis). Data were epoched to both the left and right checkerboard streams and averaged across two posterior sensor groups prior to plotting (c.f. Gray, Frey et al. 2015). Broadband, unfiltered data are given alongside a delta-filtered (1-2 Hz) equivalent. Attended (hit trials only) and unattended conditions are shown.

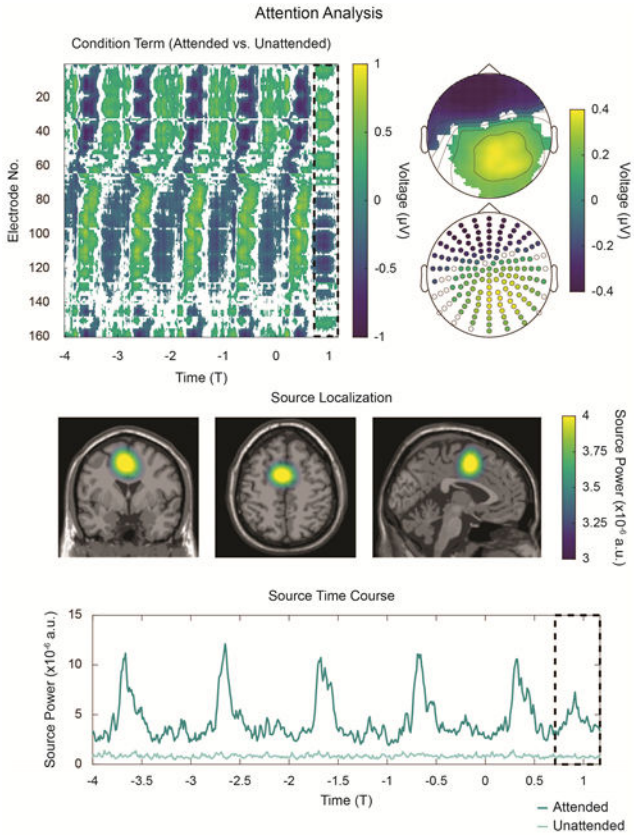

Figure 3:

Statistical and source analyses of non-filtered data in Figure 2. *Top Left*: Cluster-corrected, nonparametric statistical analysis reveals a significant main effect of attention. Data are averaged across left and right hemifield and masked by significance ($p < 0.05$). The effect is significant for both the stimulation interval ($T < 0$) and the T_1-interval, which is denoted by the black, dashed box from $T = 0.715$ to $T = 1.17$ cycles elapsed. *Top Right*: Average topographies generated from the T_1-interval, masked by statistical significance. Topographies are shown both in interpolated and scatter-plot formats for reference. *Middle*: Source-localization reveals power differences between the attended (hit trials only) and unattended conditions during the T_1-interval. Opacity masking employs the same scale as the colorbar. Other focal sources are evident (e.g. see Supplementary Figure 5, *Middle* and *Bottom*) but are here transparency masked for clarity. *Bottom*: Reconstructed power time-course of the source above. Increased source activity is observed after each checkerboard presentation; critically, increased activity is also observed in the T_1-interval.

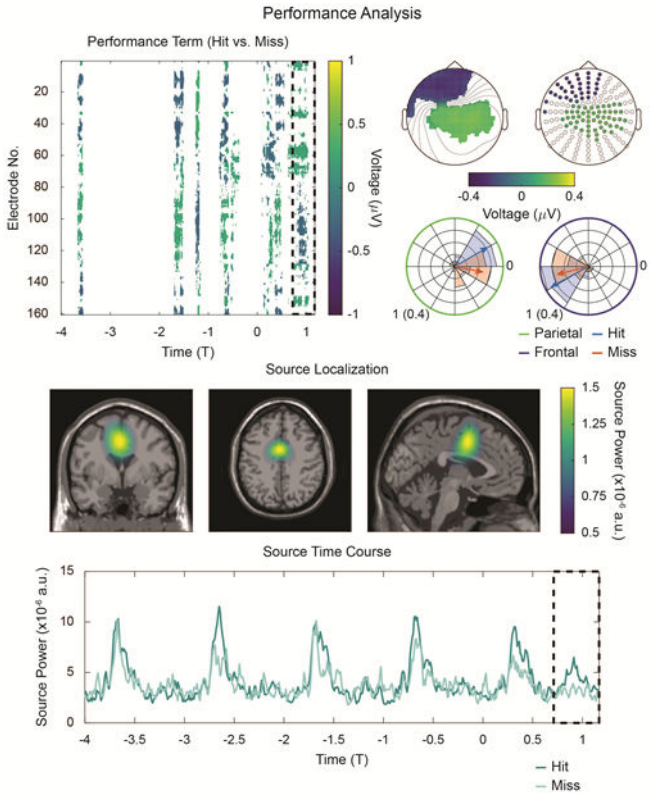

Figure 4:

Performance-related frontal activity. *Top Left*: Cluster-corrected, nonparametric randomization analysis of the main effect of performance reveals a significant effect during the T_1-interval. The difference between hit and miss conditions is plotted, masked by significance ($p < 0.05$). *Top Right*: Significance-masked topographies of the performance contrast during the T_1-interval. The two clusters of sensors shown in the scatter plot were employed to investigate phase angle of delta-activity at each cluster as a function of performance. Angular histograms and mean angles are shown. For circular plots, the radial axis is scaled to unit length for the mean angle and to a probability (0.04) for the histograms. *Middle*: Source-localized contrast between hits and misses (c.f. Figure 3, *Middle*), revealing increased source power during the hit condition. *Bottom*: As in Figure 3, *Bottom*, average source-power time-courses were extracted for each condition. During the T_1-interval, source power increases above baseline for the hit condition; no such increase over baseline is evident for the miss condition.

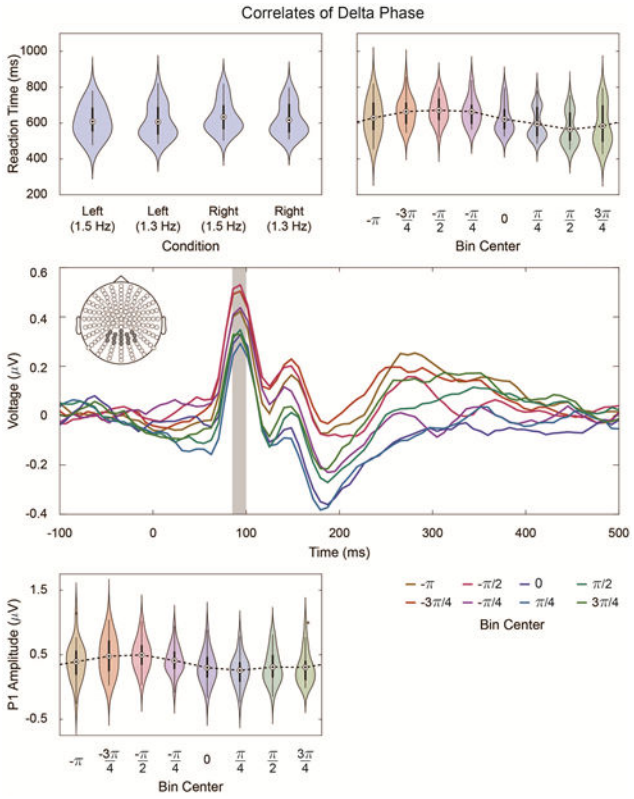

Figure 5:

Correlates of Delta Phase. *Top Left*: Average reaction time for hit trials in each condition (checkerboard hemifield × checkerboard rotation frequency). Reaction times are relative to T_1. For all violin plots, density estimation is performed with a Gaussian kernel; dots signify means, and darker bars signify the interquartile range. Lighter bars show the (non-outlier) range, where outliers are those points that lie more than 1.5 times the interquartile range outside of either the first or third quartiles. Where appropriate (e.g. *Bottom Left*), outliers are plotted separately. Repeated measures ANOVA testing reveals a small decrease in reaction times for deviants in the left hemifield ($F_{(1,22)} = 11.10$; $p = 0.003$; in ms: 95% CI [6.7,28.7]). *Top Right*: Reaction time as a function of parietal-sensor delta phase at T_1 (see Figure 4, *Top Right*, green electrodes). For each hit trial, delta-phase at T_1 is extracted, and reaction times are binned according to these phases. *Middle*: Pooled VEPs in response to presentation of the unattended checkerboards, binned as a function of parietal-sensor delta-phase (Figure 4, *Top Right*, green electrodes). VEPs are pooled across all checkerboard hemifield × rotation frequency combinations and averaged across the electrodes depicted in gray; the P1 interval is shaded from 85 to 100 ms. *Bottom Left*: Unattended P1 amplitude as a function of parietal-sensor delta phase (Figure 4, *Top Right*, green electrodes).

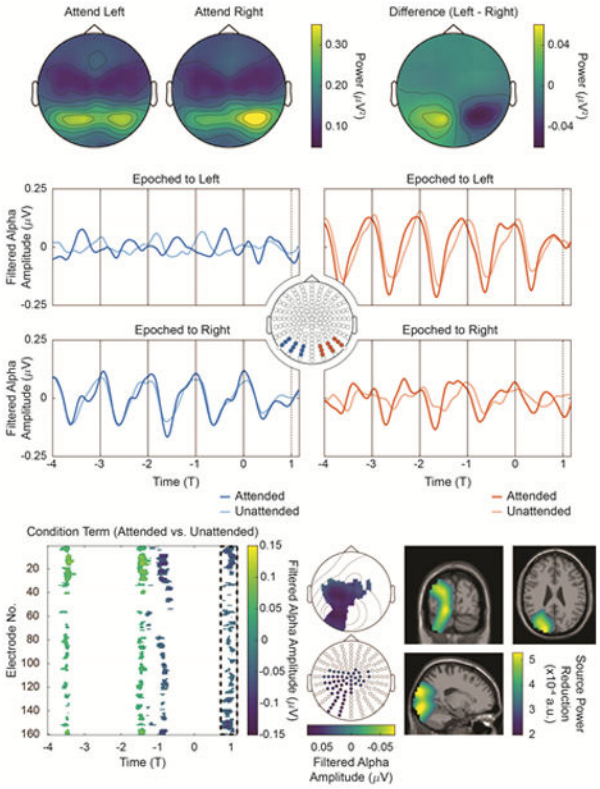

Figure 6:

Time-locked alpha envelopes. *Top*: Posterior alpha power lateralizes as a function of spatial attention. Topographies on the left show the focus of alpha power when attended left and right, respectively. The topography on the right shows the difference between the two (Attend Left – Attend Right). *Middle*: Averaged alpha envelopes, demeaned by high-pass filtering at 1 Hz; data are collapsed across stimulus configurations and shown for the both the attend left and attend right conditions for two posterior sensor groups. *Bottom Left*: Non-parametric, cluster-corrected randomization testing reveals significant differences between the attended and unattended conditions on the T_1-interval after mirroring (see text); data is masked by cluster p-value < 0.05. *Bottom Middle*: Significance-masked topographies during the T_1-interval reveal that the alpha power decrease at T_1 is localized primarily to ipsilateral sensors (i.e. left sensors post-mirror). *Bottom Right*: Source-localization with frequency-domain eLORETA show that the T_1-interval decrease in alpha power is localized primarily to ipsilateral regions. Note that opacity masking in *Bottom Right* is not on the same scale as the colorbar; instead, it goes from transparent at 2.85×10^{-4} au to fully opaque at 3.5×10^{-4} au.

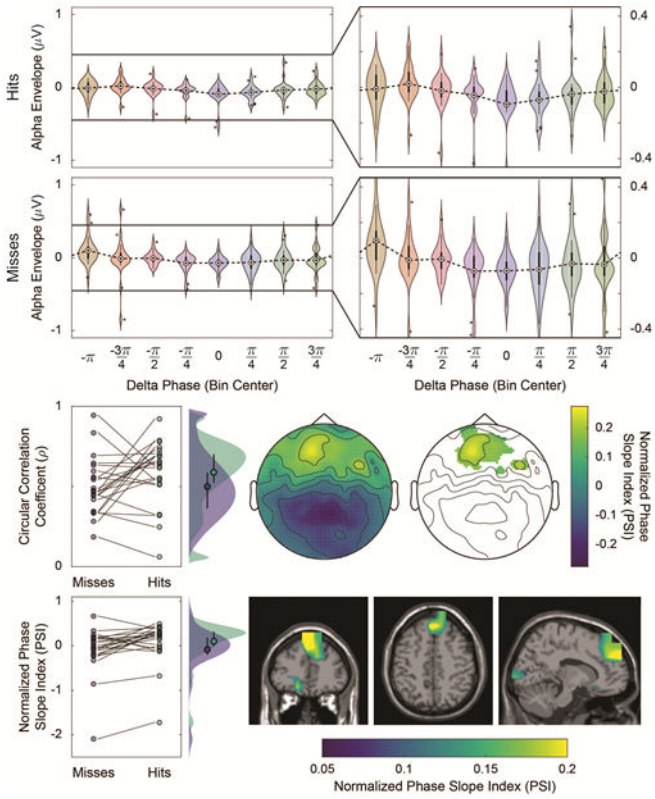

Figure 7:

Relationship between alpha amplitude and delta phase. *Top*: Comodulograms show that (high-pass filtered) ipsilateral alpha power is significantly correlated to frontal delta phase. Data is presented in violin plot format as in Figure 55. Zoomed-in violin plots are also shown for convenience. *Middle Left*: Raincloud plot of individual circular-linear correlation coefficients between the hit and miss conditions showing an increase in ρ as a function of performance (although see Supplementary Figure 10). Individual ρ values are shown by dots, and individual subject trends are shown by trendlines connecting hits and misses. Probability distributions shown to the right of the raw data are generated by convolution with a Gaussian kernel and normalized to total area 1 under the curve. Means and interquartile ranges for each condition are denoted by the markers and bars on the probability distributions. *Middle Center* and *Middle Right*: Topographies showing PSI contrast between hit and miss conditions, both with (right) and without (center) probability masking ($p < 0.05$ by nonparametric, cluster-corrected randomization testing). Positive values indicate the electrodes at which PSI is greater in the hit condition than the miss condition. Negative values indicate the opposite. The significance-masked frontal region in *Middle Right* indicates that average PSI between delta activity at these electrodes and ipsilateral alpha power correlates with task performance. *Bottom Left*: PSI values pooled over the significant electrodes in *Middle Right* were used to construct a raincloud plot as a function of condition. Raincloud plotting conventions from *Middle Left* are employed. *Bottom Right*: PSI analysis repeated in source-space. Again, a contrast between hit and miss

conditions is shown. A frontocentral source is evident, indicating that frontocentral delta activity drives ipsilateral, posterior alpha power as a function of performance.